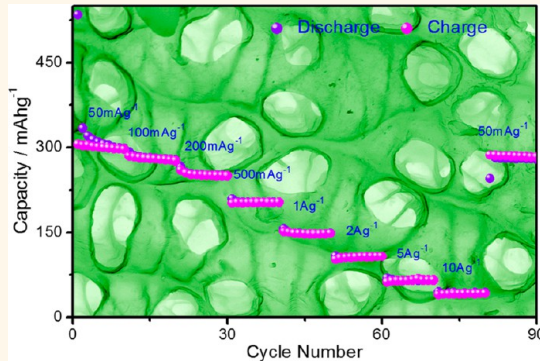


Carbon Nanosheet Frameworks Derived from Peat Moss as High Performance Sodium Ion Battery Anodes

Jia Ding,^{†,‡} Huanlei Wang,^{†,‡} Zhi Li,^{†,‡,*} Alireza Kohandehghan,^{†,‡} Kai Cui,[‡] Zhanwei Xu,^{†,‡} Benjamin Zahiri,^{†,‡} Xuehai Tan,^{†,‡} Elmira Memarzadeh Loffabadi,^{†,‡} Brian C. Olsen,^{†,‡} and David Mitlin^{†,‡,*}

[†]Chemical and Materials Engineering, University of Alberta, Edmonton, Alberta T6G 2V4, Canada and [‡]National Institute for Nanotechnology (NINT), National Research Council of Canada, Edmonton, Alberta T6G 2M9, Canada

ABSTRACT We demonstrate that peat moss, a wild plant that covers 3% of the earth's surface, serves as an ideal precursor to create sodium ion battery (NIB) anodes with some of the most attractive electrochemical properties ever reported for carbonaceous materials. By inheriting the unique cellular structure of peat moss leaves, the resultant materials are composed of three-dimensional macroporous interconnected networks of carbon nanosheets (as thin as 60 nm). The peat moss tissue is highly cross-linked, being rich in lignin and hemicellulose, suppressing the nucleation of equilibrium graphite even at 1100 °C. Rather, the carbons form highly ordered pseudographitic arrays with substantially larger intergraphene spacing (0.388 nm) than graphite ($c/2 = 0.3354$ nm). XRD analysis demonstrates that this allows for significant Na intercalation to occur even below 0.2 V vs Na/Na⁺. By also incorporating a mild (300 °C) air activation step, we introduce hierarchical micro- and mesoporosity that tremendously improves the high rate performance through facile electrolyte access and further reduced Na ion diffusion distances. The optimized structures (carbonization at 1100 °C + activation) result in a stable cycling capacity of 298 mAh g⁻¹ (after 10 cycles, 50 mA g⁻¹), with ~150 mAh g⁻¹ of charge accumulating between 0.1 and 0.001 V with negligible voltage hysteresis in that region, nearly 100% cycling Coulombic efficiency, and superb cycling retention and high rate capacity (255 mAh g⁻¹ at the 210th cycle, stable capacity of 203 mAh g⁻¹ at 500 mA g⁻¹).



KEYWORDS: sodium ion battery · lithium ion battery · carbon · graphite · graphene · pore

Advanced portable and automotive electrical energy storage (EES) systems are primarily based on lithium ion battery (LIB) technologies. However there is increasing concern about the use of lithium due to its cost disadvantage and overall global scarcity. Sodium is an attractive alternative to lithium due to its markedly lower cost and much wider global abundance. Sodium ion batteries (NIBs) are therefore attracting increasing scientific attention, particularly with regard to large-scale stationary applications where their lower gravimetric energy density is less of an issue.^{1,2}

Substantial success has been recently achieved in developing NIB cathode materials,^{3–5} with less obvious choices

being available for the anode. Researchers have developed inorganic intercalation compounds,⁶ organic compounds,⁷ or alloying metal/metal oxides^{8–10} as potential anode materials. However each class of such materials displays certain intrinsic limitations, such as a high overpotential associated with conversion reaction or alloying reaction electrodes. Carbonaceous material is a dominant candidate as electrode material for EES devices.^{11–15} Because of its desirable electrochemical attributes, graphite remains the dominant anode material for commercial LIBs.^{16,17} These attributes include a closely spaced (*i.e.*, low voltage hysteresis on charge vs discharge) voltage plateau close to Li/Li⁺,^{18,19} which for a given cathode material leads to the widest possible voltage window.

* Address correspondence to
lizhcn@gmail.com,
dmitlin@ualberta.ca.

Received for review September 4, 2013
and accepted November 5, 2013.

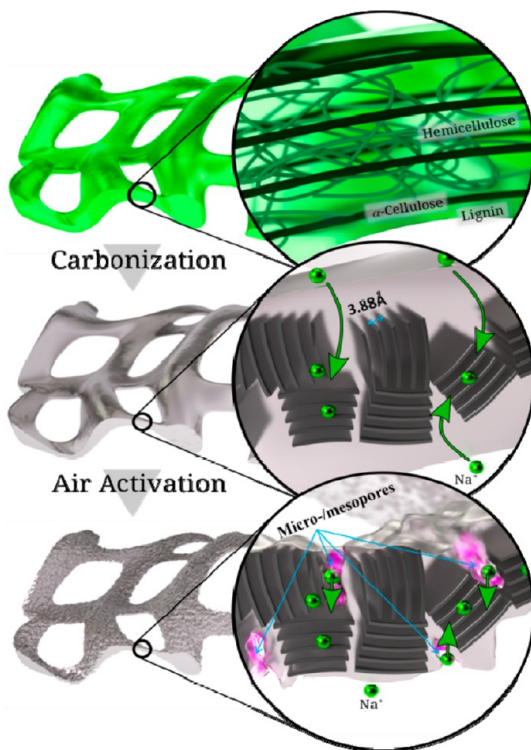
Published online November 05, 2013
10.1021/nn404640c

© 2013 American Chemical Society

Because of the minor and highly reversible dilation of the graphite lattice during lithiation/delithiation ($c/2$ changes from 3.35 to 3.6 Å), the electrodes are stable upon extensive cycling. Moreover, graphite achieves superior Coulombic efficiency due to relatively low levels of cycling-induced solid electrolyte interface (SEI) growth. A NIB anode that displays these characteristics would be very useful.²⁰

However reports of LIB-graphite analogues for NIBs are scarce. Traditional “soft” carbons with substantial turbostratic disorder display as much as 50% of the total capacity in the less useful >0.5 V range.²¹ Early work on nongraphitizable “hard” carbons demonstrated considerable capacity (200–300 mAh g⁻¹), but have unqualified cyclability and rate performance.^{22–25} Tempered carbons,²⁶ hollow carbon spheres,²⁷ and carbon nanosheets²⁸ have demonstrated improved rate performance because of their porosity. A recent study on hollow carbon nanowires derived from polyaniline reported attractive potential *versus* capacity profiles in addition to improved rate capability, the former being attributed to a combination of pore filling and a diluted graphene layer spacing.²⁹

A survey of the existing literature on carbons with optimum energy storage attributes shows that it is essential to couple the intrinsic structure of the precursor with tailored carbonization/activation treatment.^{30,31} Since no two precursors are identical, neither should be the synthesis routes designed to extract the maximum electrochemical performance. Moreover both the precursor and the synthesis process should be “green” in terms of minimal use of harmful chemicals and ideally a negative or a net zero CO₂ footprint.³² It also has to be economically viable. Peat moss is one of the most abundant plant species, with peatland (land with a naturally accumulated layer of peat moss), covering around 4 million km² of land (3% of the earth!).³³ Peat moss is also well-known for its astonishing water-holding ability due to the open macroscopic cellular structure in the leaves. As will be demonstrated, such macroscopic structure leads to very favorable electrode architectures in the postpyrolysis, postactivation specimens. Unlike the various woods that are cellulose-rich, peat moss has a high content of cross-linked polymers including hemicellulose and lignin (ca. 80 wt % total).³⁴ This would make it difficult to graphitize the majority of the material even at high carbonization temperatures.³⁵ In this work, we take full advantage of both the cellular structure and the high degree of cross-linking. Through a facile tailored synthesis process of carbonization and activation, this virtually inexhaustible biomass is converted into NIB anodes with the electrochemical characteristics approaching that of graphite when employed in lithium ion batteries.



Scheme 1. The structure changes of peat moss cell walls during carbonization and activation. The zoomed-in areas from top to bottom highlight the highly cross-linked polymer tissue in hyaline cell walls, sodium insertion in the graphitic carbon layers with expanded *d*-spacing, and the facilitated sodium ion diffusion through the micro/mesopores generated during activation

RESULTS AND DISCUSSION

The peat moss precursor is first carbonized at a range of temperatures ($T_{\text{carb}} = 600, 900, 1100, 1400$ °C) under inert atmosphere. Some of the samples were then activated under air flow at 300 °C for 3 h. The entire synthesis process, along with the initial precursor structure, the postcarbonization and activation microstructures, and the possible sodiation mechanisms, are illustrated in Scheme 1. The key linkages between all of these aspects will be discussed in the subsequent text. The as prepared carbonized peat moss is named CPM-*x*, and the further activated carbon is named CPM-*x*-A, where *x* refers to the carbonization temperature. For comparison, a commercial activated carbon (NORIT A SUPRA) labeled as CAC was also analyzed.

Figure S1A (Supporting Information) shows a macroscopic photograph of the as-received peat moss employed as the carbon precursor. The material consists of relatively coarse (mm- and cm-scale) agglomerates that could be handled by hand without disintegrating. The peat moss consists of “wound” macroscopic assemblies of leaves (termed “stem leaves”) along the main stem. The stem leaves are primarily composed of clear cells, termed hyaline cells. Because of the large volume of hyaline cells and the thin yet flexible cell walls, the peat moss delivers astonishing absorbent

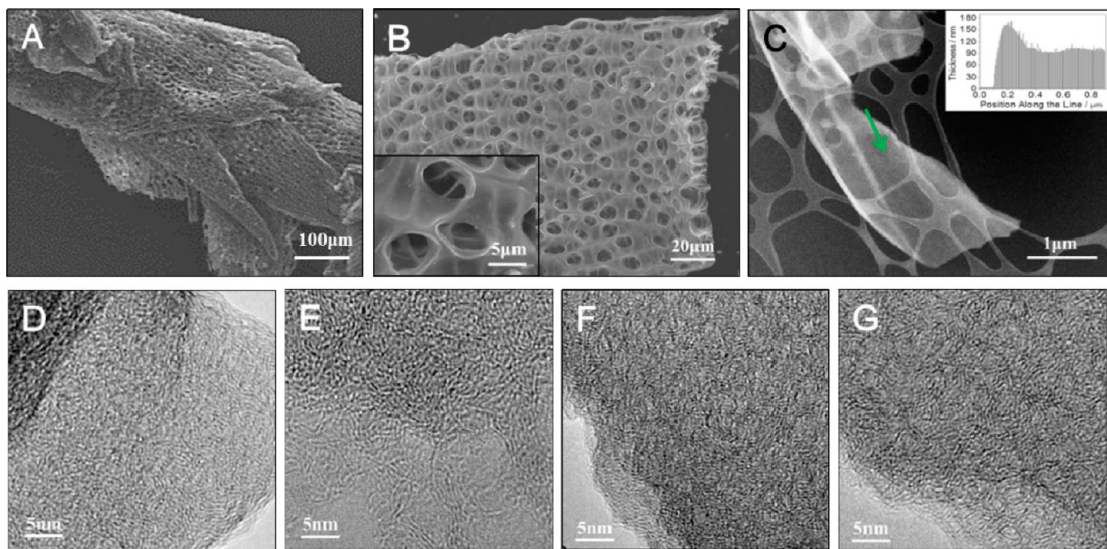


Figure 1. (A) Low magnification SEM micrograph of peat moss derived carbon (CPM-1100-A). (B) Higher magnification SEM micrograph highlighting the hollow macroporous architecture of the carbon particles (CPM-1100-A). (C) HAADF TEM micrograph and EELS thickness profile (inset) of the arrowed carbon strand in CPM-1100-A. (D–G) HRTEM micrographs of CPM-600-A, CPM-900-A, CPM-1100-A, and CPM-1400-A, respectively.

and water-holding capacity (can hold 16–26 times as much water as the dry weight),³⁶ like a sponge. The commercial products of peat moss biomass are fully dried plants that were harvested on the peatland. Water and cytoplasm in the hyaline cell were forced out, leaving only the cell wall. In the scanning electron microscopy (SEM) images of peat moss precursor (Figure S1B, Supporting Information), the shape of the hyaline cell can be observed (arrowed). The removal of the cytoplasm leaves numerous macroscopic voids, while the cell walls build up an interconnected framework. The cell walls contain *ca.* 20% in weight of α -cellulose, which is a long straight 1,4 glycosidic linkage polymer.³⁷ The α -cellulose acts as a hard scaffold conferring the mechanical strength of the whole carbon framework.³⁸ This scaffolding remains in place during pyrolysis, with the α -cellulose rich portions of the material being expected to preferentially graphitize at lower temperatures. Figure 1A shows a low magnification SEM micrograph of a peat moss leaf carbonized at 1100 °C. The final product had this type of morphology regardless of the carbonization temperature. Even when the carbonization temperature is increased to 1400 °C (Figure S2B, Supporting Information), the macroscopic carbon frameworks do not collapse.

After mechanical grinding, the larger carbon framework breaks up into irregularly shaped carbon particles that are 20–300 μm in dimensions. According to the SEM images (Figure 1B), each carbon particle displays a hollow three-dimensional architecture with linked macropores. The SEM images revealed no difference in macroscopic structures before and after activation. The unique open morphologies of the CPM specimens are fundamentally different from those of commercial

activated carbons, such as the highly popular NORIT SUPRA. Figure S2F (Supporting Information) shows the SEM micrographs of CAC particulates that are effectively 3D micrometer-scale clumps without any open structure to facilitate electrolyte penetration and ion diffusion. As will be demonstrated, the intrinsic macroscopic openness of CPM specimens is one essential feature for optimum material utilization during sodium insertion/extraction.

Figure 1C and Figure S2D,E (Supporting Information) show high angle annular dark field (HAADF) transmission electron microscopy (TEM) micrographs and electron energy loss spectroscopy (EELS) thickness profiles of the CPM-A specimens. The carbon walls derived from the hyaline display thicknesses between 60 and 180 nm, with such location-to-location thickness variations being encountered in all the CPM specimens. The resultant Na diffusion distances are at the maximum of 1/2 of those thicknesses (there is electrolyte contact on both sides of the macropores). Moreover these air-activated specimens contain micro- and mesopores that actually further reduce the diffusion distances due to electrolyte penetration.

The low carbonization temperature specimen (CPM-600-A) displays highly disordered structure, with limited evidence of any graphitic nanocrystallites. The contrast displayed in the HRTEM micrograph of this material, shown in Figure 1D, agrees with the interpretation that such structure is primarily amorphous with any “graphitic” domains being sub-2 nm in scale.³⁹ With increasing carbonization temperature, the material becomes progressively more ordered. Figure 1E shows the HRTEM micrograph of the CPM-900-A specimen, while Figure 1F shows the CPM-1100-A sample, which will be demonstrated to possess optimum

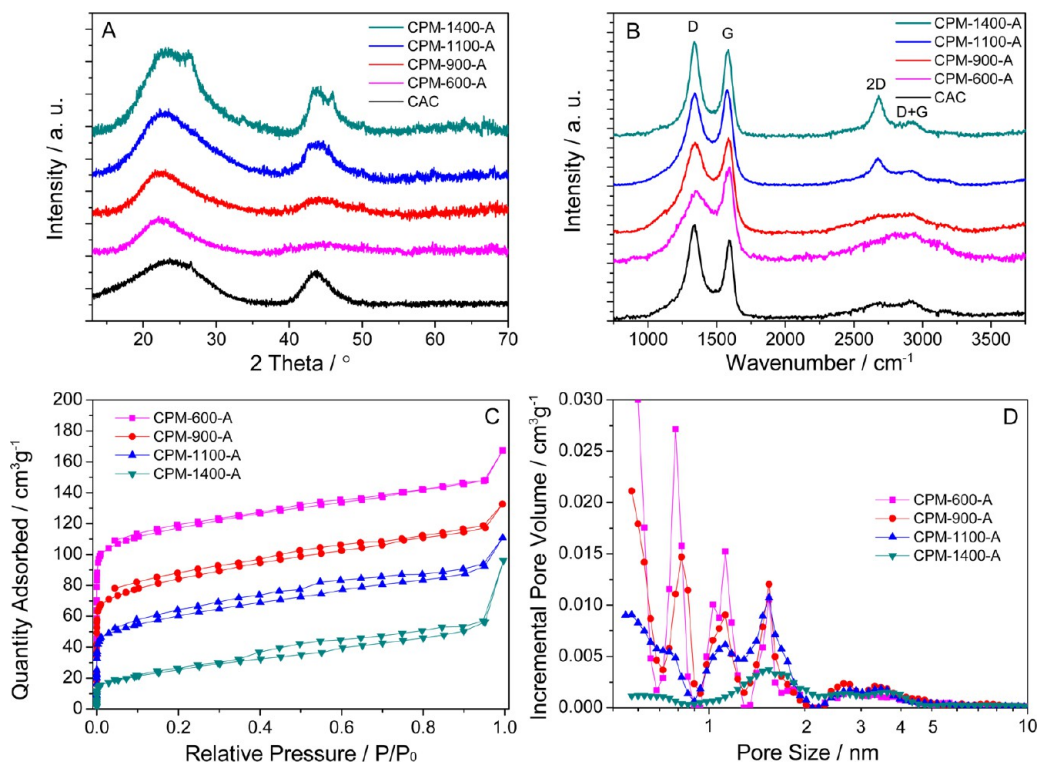


Figure 2. (A) XRD patterns of the activated specimens (CPM-A) and of commercial activated carbon (CAC). (B) Raman spectra of CPM-A and CAC. (C) Nitrogen adsorption–desorption isotherms of CPM-A. (D) Pore size distribution calculated from the adsorption isotherms, using DFT method.

electrochemical properties. The CPM-1100-A specimen shows evidence of substantial local order, though without the presence of equilibrium graphite phase. The CPM-1400-A specimen (Figure 1G) is highly ordered. As Raman and XRD will demonstrate, the material is now actually partially graphitic, with the domains containing graphite of equilibrium interplanar spacing. All the specimens show HRTEM contrast consistent with what is typically reported for micro-porous and mesoporous carbons. However we believe that due to ambiguities created by the inevitable pore and material overlap in the TEM specimens, nitrogen sorption analysis, discussed next, is more effective in identifying the porosity.

Figure 2A shows the X-ray diffraction (XRD) patterns of the CPM-A specimens along with those of baseline CAC. The XRD patterns of the CPM specimens are shown in Figure S4A (Supporting Information). The results of the XRD analysis, along with the results of Raman and BET, are shown in Table 1. The average graphene interlayer spacing was calculated from the peak centers. The thickness and average width of the graphitic domains, L_c and L_a , are calculated based on the well-known Scherrer equation, using the fwhm values of (002) at $2\theta \sim 23^\circ$ and (100) at $2\theta \sim 43^\circ$. In the case of the CPM-1400-A there are two overlapping peaks at each position, which may be readily mathematically deconvoluted using the Voigt function. It can be seen that the 300 °C activation will not appreciably

alter the graphitic order/disorder. In all but the 1400 °C specimens, the average thickness of the graphitic domains is ~ 1.8 nm, indicating that they are composed of 4–5 stacked graphene layers (*i.e.*, $1.8/0.38 = 4.7$).^{40,41} As Table 1 demonstrates, the intergraphene layer spacing (d_{002}) gradually shifts toward lower values with increasing carbonization temperature. However, a comparison of the 600, 900, and 1100 °C specimens indicates that this trend is quite weak, and that in all cases the spacing is significantly above that of equilibrium graphite (0.3354 nm). Carbonizing at 1400 °C creates a clear bimodal distribution in the average d spacings, indicating that finally the temperature is high enough to form equilibrium graphite ($c/2$ measured as 0.334 nm). On the basis of the ratio of the deconvoluted areas of the peak doublets, the carbon to equilibrium graphite ratio is 4:1 by weight. Interestingly the remaining carbon maintains a dilated intergraphene spacing (0.383 nm), indicating that the formation of graphite occurs *via* nucleation and growth rather than by ordering and shrinkage of the existing lattice. Since the peat moss precursor is heterogeneous, graphite would be expected to form preferentially in regions originally rich in α -cellulose. For CPM-600-A, CPM-900-A, CPM-1100-A, the average value of interlayer spacing are 0.399, 0.395, 0.388 nm, respectively. Such open structures are known to allow for facile Na insertion/extraction between the graphene planes.²⁷ What is unique about the 1100 °C specimen is that despite

TABLE 1. Physical Parameters and Electrochemical Properties for CPM, CPM-A, and CAC

samples	d_{002} (Å)	L_a (nm)	L_c (nm)	I_G/I_D ^a	S_{BET} (m ² g ⁻¹) ^b	V_t (cm ³ g ⁻¹) ^c	pore		pore		C_{50} mA g ⁻¹ ^d	C_{500} mA g ⁻¹ ^e
							vol % (<2 nm)	vol % (>2 nm)	(mAh g ⁻¹)	(mAh g ⁻¹)		
CPM-600	3.98	1.83	1.80	0.51	55.3	0.069	46.1	53.9	230	93		
CPM-900	3.91	2.52	1.79	0.76	45.1	0.059	24.2	75.8	219	91		
CPM-1100	3.87	5.11	1.83	0.87	24.5	0.054	4.5	95.5	325	117		
CPM-1400	3.82/3.34	8.36/16.21	1.90/6.31	0.89	20.8	0.052	10.7	89.3	275	84		
CPM-600-A	3.99	1.75	1.80	0.47	369.1	0.26	72.7	27.3	267	150		
CPM-900-A	3.95	2.85	1.83	0.71	271.2	0.21	64.7	35.3	280	155		
CPM-1100-A	3.88	5.39	1.86	0.86	196.6	0.18	47.9	52.1	332	203		
CPM-1400-A	3.83/3.34	8.51/17.18	2.21/6.25	0.91	92.2	0.12	25.2	74.8	294	139		
CAC	3.72	4.2	1.84	0.26	2050	1.17	61.7	38.3	139	38		

^a I_D and I_G are the integrated intensities of D- and G-band. ^b Surface area was calculated with Brunauer–Emmett–Teller (BET) method. ^c The total pore volume was determined at a relative pressure of 0.98. ^d Discharge capacity at the 2nd cycle. ^e Reversible capacity at the 35th cycle in the rate tests.

having a mean spacing far above that of graphite the material is quite ordered, having a mean graphitic domain width of over 5 nm. The only specimen that shows larger domain dimensions is CPM-1400-A, though it is composed of 20% electrochemically inactive graphite. The baseline CAC possesses comparable domain widths (4 nm), but has a smaller graphene interlayer thickness (0.372 nm). As Raman results will demonstrate, it is also much less ordered/more defective. These attributes, combined with ion diffusional limitations associated CAC's closed particulate morphology, will hinder Na ion transfer and tremendously place it at an electrochemical performance disadvantage.

Raman spectroscopy analysis was employed to investigate the structure of the CPM-A specimens. These results, along with the same analysis performed on CAC, are shown in Figure 2B. All samples exhibit a broad disorder-induced D-band (≈ 1340 cm⁻¹) and in-plane vibrational G-band (≈ 1580 cm⁻¹). The integral intensity ratio (I_G/I_D) is indicative of the degree of graphitic ordering in the carbons.⁴² The fits of the spectra are shown in Figure S3 (Supporting Information).⁴³ As shown in Table 1, increasing the carbonization temperature to 1400 °C leads to a progressively more ordered structure. The 2D peak at ≈ 2680 cm⁻¹ may also be used as a measure of order.^{44–46} These are only prevalent in the 1100 and 1400 °C specimens. The CAC specimens are markedly less ordered than any of the CPM. To contrast, for CPM-1100-A and CPM-1400-A the ratio $I_G/I_D = 0.87$ and 0.91, while for CAC the ratio is 0.26.

During the carbonization process, a material composed of primarily α -cellulose would readily graphitize at high temperature because of the long-scale parallel fashion of the linear polysaccharide ($C_6H_{10}O_5$)_n chains.⁴⁷ However the main components (ca. 80 wt %) of peat moss are actually hemicellulose (β -, γ -cellulose) and lignin. Unlike α -cellulose, the polysaccharide chain of hemicellulose is much shorter and bifurcates with glycosidically bound branches. Lignin is a three-dimensional, highly cross-linked polyphenolic polymer without any ordered repeating units.⁴⁸ The organization of

TABLE 2. Elemental Composition Information for CPM, CPM-A, and CAC

samples	elemental analysis				XPS		
	C	O	N	H	C	O	N
CPM-600	76.38	13.06	3.45	2.11	82.76	13.35	3.89
CPM-900	84.59	8.02	1.2	1.07	89.01	9.59	1.40
CPM-1100	87.11	4.93	1.03	0.51	93.65	5.28	1.07
CPM-1400	93.35	2.98	0.74	0.29	95.03	3.94	1.03
CPM-600-A	78.85	14.01	3.67	2.21	81.54	15.24	3.22
CPM-900-A	86.38	8.63	1.46	1.19	87.45	11.42	1.13
CPM-1100-A	89.35	5.13	1.05	0.49	93.41	5.84	0.75
CPM-1400-A	93.31	2.68	0.72	0.27	96.29	3.12	0.59
CAC	94.12	4.34	0.12	0.43	95.35	4.65	~0

the different polymers in the cell walls of peat moss is also shown in Scheme 1. The small amounts of long cellulosic microfibrils (α -cellulose) are imbedded in a matrix of interwoven polysaccharides. Shorter branched hemicelluloses increase the linkage among long cellulosic fibers. High content of lignin (ca. 50 wt %) fills the spaces between cellulose and hemicellulose and covalently links to the cellulose and other polysaccharides within the cell wall.^{49,50} In short, despite being heterogeneous, the overall peat moss structure is highly cross-linked and noncrystalline, which prevents graphitization at low and moderate temperatures.

Figure 2C shows the nitrogen adsorption–desorption isotherms CPM-A, while Figure 2D shows their resultant pore size distributions (obtained by density functional theory (DFT)). The same analysis for the CPM specimens and for CAC baseline are shown in Figures S5 and S6 (Supporting Information). All the adsorption curves of the CPM-A specimens display type I/IV isotherms. Table 1 shows the calculated BET surface area, and the fraction of pores that are microporous versus mesoporous. It can be seen that while air activation does increase the amount of micro- and mesoporosity in all specimens, it is progressively less effective for the

more ordered/graphitic specimens. This is not unusual since graphitic carbons are known to resist oxidation better than amorphous ones.^{51,52} All the resultant materials, however, are of relatively low surface area, ranging from 55 to $21\text{ m}^2\text{ g}^{-1}$ for CPM and from 369 to $92\text{ m}^2\text{ g}^{-1}$ for the CPM-A. To contrast, the surface area of CAC is $2050\text{ m}^2\text{ g}^{-1}$. Comparing CAC to CPM-1100-A, one observes almost an order of magnitude higher volume of micropores ($0.722\text{ vs }0.086\text{ cm}^3\text{ g}^{-1}$) and a factor of 5 higher volume of mesopores ($0.448\text{ vs }0.093\text{ cm}^3\text{ g}^{-1}$)

Table 2 presents the combustion elemental analysis and X-ray photoelectron spectroscopy (XPS) results for the specimens, listing the weight percentages of the main elements (C, O, N, H). There is a significant content of heteroatoms both on the surface (XPS) and in the bulk (elemental) of the specimens carbonized at 600 and 900 °C. XPS also shows that activation further oxidizes the surface of these more disordered carbons but has little effect on the surface composition of the 1100 and 1400 °C specimens. As expected, with increasing carbonization temperature there is a significant decrease in the carbons' oxygen, nitrogen, and hydrogen content. The CPM-1100 and CPM-1100-A specimens show comparable oxygen and hydrogen levels to CAC. While their nitrogen content (1.05 wt % bulk, 0.75 wt % surface for CPM-1100-A) is higher than CAC, it is still relatively negligible in terms of its effect on the electrochemical properties.

To investigate the electrochemical energy storage properties of the carbons we performed cyclic voltammetry (CV) and galvanostatic discharge/charge cycling. The specimens were tested between 0.001 and 2.8 V vs Na/Na⁺. Figure 3A,B shows the CV curve and discharge/charge profile of CPM-1100-A. The inset of Figure 3B presents the derivative curves dQ/dV vs V , which have a similar shape to the CV's. The galvanostatic and CV data for the other CPM-A specimens is shown in Figure S8 (Supporting Information), while the galvanostatic data for the CPM specimens is shown in Figure S9 (Supporting Information). In the first CV scan, two broad cathodic peaks are visible at ~ 0.4 and 0.75 V, disappearing in the subsequent cycling. These peaks are generally attributed to the decomposition of the electrolyte and the formation of SEI layer on the carbon surface.²⁹ The formation of SEI and any irreversible insertion of Na into the carbon structure are the main reasons for the initial irreversible capacity loss. At the low voltage region, there is a sharp cathodic peak near 0 V and a counterpart anodic peak at 0.15 V, resembling the cycle voltammetry behavior of lithium insertion/extraction in graphite.⁵³ Besides the sharp peaks, there is also a pair of weak humps over a wide voltage region (0.2–1.2 V) in both the cathodic and the anodic portions. These pairs of sharp peaks and weak humps correspond to the plateau regions and the sloping regions of the galvanostatic discharge/charge profiles, respectively.

As shown in Figure 3B, for CPM-1100-A the first cycle delivered specific capacities are 532 mAh g^{-1} (discharge) and 306 mAh g^{-1} (charge). After 10 cycles, there is still 298 mAh g^{-1} reversible capacity remaining. This cycling performance may be considered quite outstanding, since there are very few reports of carbonaceous materials displaying over 250 mAh g^{-1} of stable capacity as a NIB anode.^{28,29} The carbonization temperature has a profound effect on the shape of the voltage *versus* capacity profiles. In general, a sloping voltage plateau is associated with ion insertion into a material where the insertion sites possess a distribution of energies. A more disordered carbon would possess a wide site energy distribution, and hence would show a substantial fraction of its total capacity at higher voltages. This is the trend that we observe with CPM, with both the total amount and the relative fraction of the charge storage capacity measured above 0.2 V decreasing with I_G/I_D (Table 1 lists I_G/I_D). In CPM-1100-A, a reversible charge/discharge capacity of 196 mAh g^{-1} (after 10 cycles at 50 mAh g^{-1}) can be obtained within a narrow voltage window of 0.001–0.2 V. This is demonstrated in Figure 3C, which shows both the charging and the discharging results.

As discussed in the introduction, this low voltage/low hysteresis plateau behavior resembles the highly attractive capacity *versus* potential profiles of graphite anodes in LIB. Moreover, examining the capacity below 0.2 V (Figure 3B including insert, Figure S8, Supporting Information) it can be observed that both CPM-1100-A and CPM-1400-A behave quite on par with LIB graphite in terms of displaying almost a negligible charge/discharge voltage hysteresis.

Figure 3C shows the potential profiles of CPM-A and CAC specimens. The same type of chart is shown in Figure S10 (Supporting Information) for the CPM specimens. For CPM-A (and CPM) with increasing carbonization temperature there is an increasing capacity plateau at the low voltage region. This is interesting and somewhat unexpected since this trend is completely opposite of what one would expect if the low voltage plateau was based on filling of pores by Na metal ("nanopore filling"). As Table 1 demonstrates, the porosity in the CPM-A decreases with increasing carbonization temperature. Moreover the CAC samples are highly porous ($2050\text{ m}^2\text{ g}^{-1}$), containing both micropores and mesopores in a volume ratio of 1.6:1. Yet, the reversible capacity of CAC is low and a voltage plateau is nonexistent. Where there is a strong trend, however, is between the total capacity and "flatness" of the low voltage plateaus in CPM and CPM-A, *versus* the degree of ordering in these carbons (I_G/I_D in Table 1). The CAC specimen also fits this trend, being the least ordered of the carbons tested. This phenomenon may be explained by arguing that the more ordered domains would provide Na insertion sites that are more

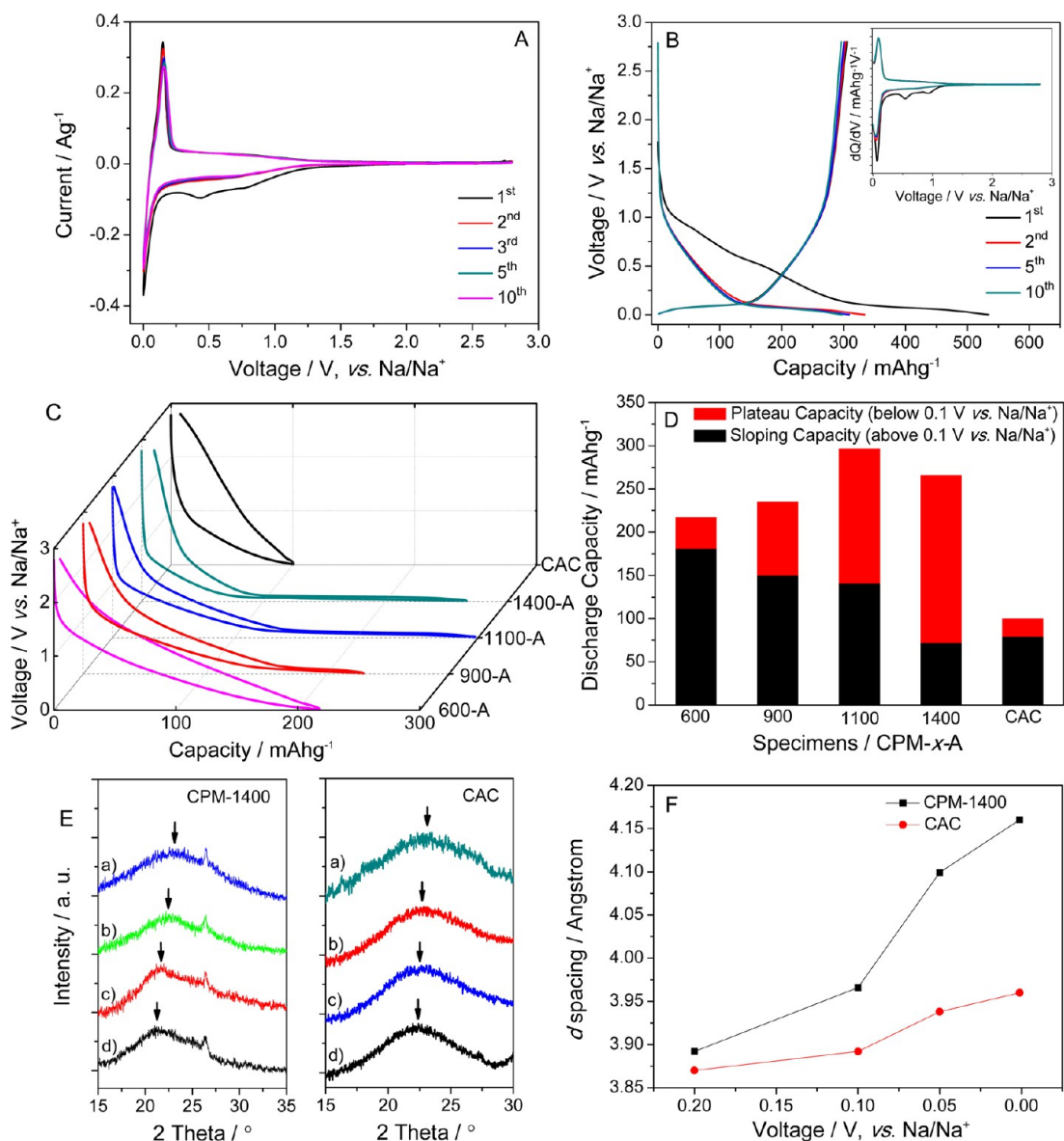


Figure 3. (A) Cyclic voltammogram of CPM-1100-A electrode between 0.001 and 2.8 V at a scanning rate of 0.1 mV s^{-1} . (B) Galvanostatic discharge/charge curves of CPM-1100-A electrode at current density of 50 mAh g^{-1} . (C) Potential profiles of CPM-A and commercial activated carbon electrodes. (D) Summary of capacity potential distribution of CPM-A and commercial activated carbon electrodes. (10th cycle at current density of 50 mAh g^{-1} in both C, D). (E) XRD spectra for CPM-1400 and CAC electrodes, demonstrating Na intercalation-induced dilation of the interlayer spacing in the majority pseudographitic phase of CPM-1400. The peaks at $2\theta = 26.4^\circ$ are for the secondary equilibrium graphite phase also present in CPM-1400, which is inactive and hence remains invariant with voltage. The electrodes were galvanostically discharged to (a) 0.2, (b) 0.1, (c) 0.05, and (d) $0.001 \text{ V vs. Na}/\text{Na}^+$. (F) Dependence of the mean interlayer spacing on discharge voltage; values derived from (E).

energetically equivalent, and hence lead to progressively flatter plateaus. Effectively the carbons would become “pseudographitic” to Na^{54} offering a chemically similar environment while maintaining a sufficiently diluted interlayer spacing to allow insertion/extraction. The progressive elimination of heteroatoms with increasing carbonization temperature would also help in establishing energetic equivalence of sites, though as demonstrated by the relatively pure CAC this criterion is by itself insufficient. The structure/performance of CPM-1400-A specimen is somewhat obscured by the roughly 20% graphite present in

the material. Nevertheless the overall trend is unambiguous.

This trend is also summarized in histogram shown in Figure 3D, where the fraction of the total capacity associated with the plateau below 0.1 V increases with CPM carbonization temperature (16% for CPM-600-A, 36% for CPM-900-A, 53% for CPM-1100-A, 73% for CPM-1400-A). Identical trend is observed for the CPM-600, CPM-900, CPM-1100 and CPM-1400 specimens (Figure S10B, Supporting Information), despite none of them containing significant porosity. In fact considering 100% pore filling by Na in the unactivated

CPM specimens (in our opinion a highly optimistic assumption), one obtains capacities of 78, 66, 61, and 54 mAh g^{-1} , for the CPM-600, CPM-900, CPM-1100, and CPM-1400. This is opposite in trend to the measured low voltage capacities. These values also do not account for the total low voltage measured capacities in CPM-900, CPM-1100, and CPM-1400. Conversely the low voltage capacity due to complete pore filling of CAC should be 1317 mAh g^{-1} , which is more than 1 order of magnitude higher than its capacity throughout the entire voltage range. While some nanopore filling by Na almost certainly occurs for all these materials at low voltages, the data leads us to hypothesize that this is not the dominant charge storage mechanism between 0.1 and 0.001 V.

Rather, we argue that because the peat moss carbons possess a unique highly ordered pseudographitic structure but with a dilated graphene interlayer spacing, it is possible to achieve significant Na intercalation down to the discharge voltage. To prove this point we carried out XRD analysis to track the structural changes in CPM within the voltage region of 0.2–0.001 V, performing identical experiments on CAC as a baseline. To obtain a “steady-state” microstructure, the half-cells first received 10 galvanostatic charge–discharge cycles at 0.1C. Upon cycle 11, the electrodes were discharged to (a) 0.2, (b) 0.1, (c) 0.05, and (d) 0.001 V. The cells were then disassembled in a glovebox with the active material being removed from the current collector, cleaned, and immediately analyzed. Specimen CPM-1400 was analyzed because of its most ordered structure of all the CPM specimens, and its largest plateau capacity (162 mAh g^{-1} below 0.1 V vs Na/Na⁺). Moreover the distinct and sharp (002) Bragg peak from the equilibrium graphite phase within this sample, being completely sodium inactive, served as a highly useful secondary *in situ* calibration standard.

Figure 3F shows the raw XRD data for CPM-1400 and the CAC samples, the broad (002) pseudographitic peaks being marked by arrows. The clearly discernible shift to lower 2θ values with decreasing terminal discharge voltage reflects the increasing intergraphene spacing due to Na intercalation. Figure 3E plots the calculated mean interlayer spacing as a function of voltage. As CPM-1400 was discharged from 0.1 to 0.001 V, the interlayer spacing expanded from 3.96 to 4.16 Å. Since the structure was highly ordered, the sodium occupation sites were energetically similar, leading to the observed flat voltage profile not unlike that of Li in graphite. To contrast, within the same voltage range the highly disordered CAC sample demonstrated a much lower interlayer dilation, going from 3.91 Å at 0.1 V to 3.96 Å at 0.001 V.

Figure 4A shows the cycling capacity retention performance of CPM-A specimens. The same plot is presented for CPM in Figure S11 (Supporting Information). The first 10 cycles were tested at a current density of

50 mA g^{-1} , and the subsequent 200 cycles were tested at 100 mA g^{-1} . As can be observed, CPM-1100-A and CPM-1100 specimens deliver the overall most favorable combination of total capacity and capacity retention, with CPM-1100-A being overall the best. The CPM-1400-A not only provides lower overall capacity but degrades at higher rates. Accelerated degradation may be perhaps related to cycling-induced growth of graphite domains at the expense of the active carbon. Alternatively pores may provide a secondary benefit of buffering the sodiation-induced expansion/contraction in the material. With much lower porosity levels, CPM-1400-A may therefore partially disintegrate during cycling.

After 10 cycles at 50 mA g^{-1} the CPM-1100-A specimen demonstrates a reversible capacity of 298 mAh g^{-1} . Over the subsequent 200 discharge/charge cycles at 100 mA g^{-1} , this value decreases to 255 mAh g^{-1} . Table S2 (Supporting Information) compares the cycling and rate performance behavior of our materials with several state-of-the-art carbons reported in literature. For preparing this comparison, we chose what were to our knowledge the best performing materials at that time. As can be seen, the CPM-1100-A carbon offers some of the best overall capacity and cycling capacity retention combinations.

The volume of the electrode is also a key consideration for a real packed cell. Figure S12A (Supporting Information) provides the volumetric capacity of CPM-1100-A as a function of cycle number. These values were obtained by dividing the measured gravimetric capacity by the electrode packing density (0.62 g cm^{-3}). The electrode had a mass loading of 1.2 mg and a geometric area of 1.13 cm^2 . The thickness of the electrode was 17 μm , being obtained from a cross section SEM image (Figure S12B, Supporting Information) and confirmed using a high precision micrometer. Figure S12A (Supporting Information) demonstrates that at a rate of at 50 mA g^{-1} the CPM-1100-A electrode displays a stable cycling capacity of approximately 200 mAh cm^{-3} , which is a promising volumetric energy value for practical NIBs applications.

The cycle 1 Coulombic efficiency increased from 43.9% for CPM-600-A, to 50.1% for CPM-900-A, to 57.5% for CPM-1100-A, and 60.1% for CPM-1400-A. Similarly cycle 1 Coulombic efficiency increased from 46.1% for CPM-600, to 55% for CPM-900, to 60.7% for CPM-1100, and 64.3% for CPM-1400-A. Of course a progressively decreasing surface area with carbonization temperature (less SEI formation) plays a role in this trend. However the analogous behavior of the low surface area CPM specimens indicates that a progressively lower heteroatom content (discussed in ref 55) is also critical in reducing the cycle 1 capacity loss. The initial columbic efficiencies CPM-1100-A and CPM-1400-A are actually somewhat higher than the counterpart values reported for high performance carbonaceous materials

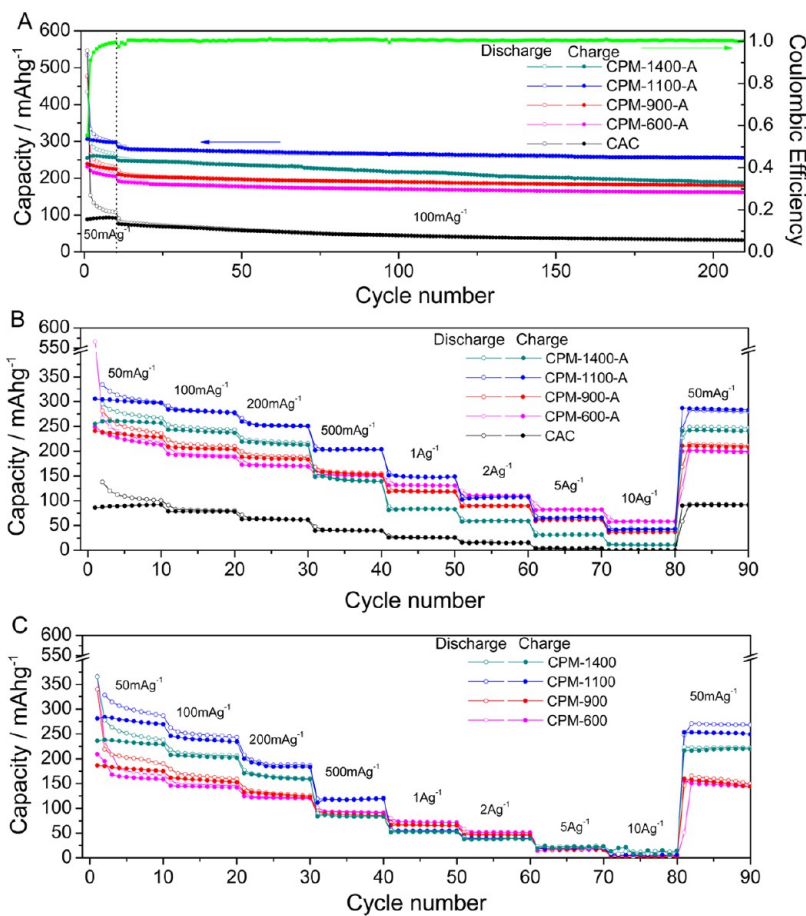


Figure 4. (A) Extended cycling performance of the CPM-A and CAC electrodes, with Coulombic efficiency of CPM-1100-A electrode being displayed. (B) Rate performance of CPM-A and CAC electrodes. (C) Rate performance of CPM electrodes.

with even lower surface areas.^{29,56} This supports the argument for the attractiveness of our materials as NIB anodes. The more ordered, less defective graphitic structures may also reduce the extent of the irreversible capacity loss reactions in the first cycle, though the exact mechanism needs clarification. In CPM-1100-A the coulombic efficiency increases rapidly to over 90% in the second cycle and stabilizes at ~100% (within measurement accuracy) from the eighth cycle onward. Figure 4A (right axis) shows the Coulombic efficiency for the CPM-1100-A specimens during cycling. An analogous trend is observed for all but the CPM-1400 specimens, with ~100% efficiency being measured during stable cycling. CPM-1400 however never quite reaches 100% efficiency, performing between 98–99% for the majority of the cycling.

Figures S14 and S15 (Supporting Information) show the electrochemical impedance spectra (EIS) analysis of the CPM and CPM-A specimens. Figure S14A (Supporting Information) shows the Nyquist of CPM, CPM-A and CAC specimens before cycling. Figure S14B (Supporting Information) shows the same analysis but after 210 cycles. The value of $R_{ct} + R_f$, simulated from the fit of the experimental Nyquist plots with the equivalent circuit shown in Figure S13B (Supporting

Information), represents the combination of charge transfer resistance at the SEI/electrolyte interface and the resistance of Na transport through SEI layer.⁵⁷ It is the physically meaningful parameter for analysis of the cycled specimens, which is expected to increase with SEI growth. In LIB applications of graphite materials a substantial rise in $R_{ct} + R_f$ would mean that the initially low surface area electrode was creating new surfaces for SEI formation (SEI preferentially forms of fresh carbon surfaces exposed to the electrolyte rather than on the back of existing SEI), by exfoliating and/or fracturing.⁵⁸ Similarly for high surface area carbons, a cycling induced increase in $R_{ct} + R_f$ signifies some form of material disintegration. While SEI growth in NIB applications is less well understood, a qualitatively similar scenario may be expected. The CPM-1400 and CPM-1400-A specimens have the largest % increase in $R_{ct} + R_f$ versus the initial R_{ct} . These are also the specimens that demonstrate the highest rate of capacity degradation during cycling. Of all the specimens CPM-1100-A shows the lowest value of $R_{ct} + R_f$ (114.7 Ω), indicating that it is the most stable against SEI growth during cycling. For CPM-1100 $R_{ct} + R_f$ is 350.4 Ω . The difference between CPM-1100-A and CPM-1100 supports the argument that

pores buffer sodiation-induced expansion/contraction (*i.e.*, damage) in the matrix.

Figure S15A,B (Supporting Information) shows the change of $R_{ct} + R_f$ and R_{el} as a function of cycle number in CPM-1100-A and CPM-1400-A electrodes. Figure S15C,D (Supporting Information) shows the raw Nyquist plots in the as-prepared electrodes and after 30, 100, 150, and 210 cycles. As shown in Figure S15A (Supporting Information), the much slower increase of $R_{ct} + R_f$ in CPM-1100-A with increasing cycle number indicates a more stable SEI layer throughout cycling. A stable SEI is known to promote high capacity retention²⁷ and is likely related to the microstructural features of CPM-1100-A *versus* CPM-1400-A previously discussed.

Where the really interesting difference between the CPM and CPM-A specimens emerges is in their rate capability, shown in Figure 4B,C. At high charge rates, such as at 2 and 5 A g⁻¹, the unactivated samples show effectively negligible capacity. Conversely the CPM-1100-A, CPM-900-A, and CPM-600-A all still perform. The CPM-1100-A specimens provide stable capacities of 203 mAh g⁻¹ at 500 mA g⁻¹, 150 mAh g⁻¹ at 1 A g⁻¹, 106 mAh g⁻¹ at 2 A g⁻¹, and 66 mAh g⁻¹ at 5 A g⁻¹, rates over 1 A g⁻¹ being considered very high (*e.g.*, assuming a capacity of 200 mAh g⁻¹, 1 A g⁻¹ is equal to 5 Ci).

As we argued earlier in the text, the introduction of limited porosity will in effect reduce the required Na ion diffusion distances since the electrolyte will be able to penetrate into the pores. Where this seems to matter the most is at high rates, where it is logical to surmise that Na diffusion in the *bulk* of the carbon may be the rate limited step. Solid-state diffusion of ions has been argued to be the limiting factor for the high rate performance of bulk intercalation electrodes.^{4,5,8,59} The activation process would not affect the solid-state diffusion values of Na in carbon, but could substantially reduce the diffusion distances necessary for full sodiation of the material. Since time is proportional to the diffusion distance squared (Fick's first law), if all else being equal, thinner walls of carbon would sodiate

faster. The CPM-1400-A samples have by far the lowest surface area of all the activated specimens (less than 1/2 the surface area of CPM-1100-A), indicating less penetrating porosity and explaining the worse rate capability. Were nanopore filling to become an important Na storage mechanism in the specimens at high charge/discharge rates, activation would similarly facilitate increased capacity. Comparing the CPM-1100-A specimens to the carbons presented in Table S2 (Supporting Information) demonstrates its highly promising rate capability, on par with the more exotic open structures such as hollow carbon spheres and carbon nanosheets. In fact for a given current density in the range of 0.2–2 A g⁻¹, CPM-1100-A exceeds all the counterpart capacities.

CONCLUSION

In this study we synthesized and tested carbons derived from a ubiquitously found biomass precursor, namely peat moss. Taking advantage of the cross-linked organization of the polymers in the peat moss cell wall, we achieved highly ordered pseudographic structures with a highly dilated graphene interlayer spacing. This allowed for facile Na intercalation into the carbons' bulk, while the high level of order created a chemically homogeneous environment for the inserted ions and hence relatively flat voltage profiles. The intrinsically open macroporous structure of the peat moss resulted in sheet-like walls in the postpyrolyzed carbons that were as thin as 60 nm. To improve the high rate performance we employed mild air activation (300 °C) to create sufficient porosity to further reduce the Na diffusion distances. The resultant carbons display superb (some of the best reported in literature) electrochemical performance in numerous respects, including total reversible capacity, cycling stability, rate capability, charge/discharge voltage hysteresis. The exceptional performance, combined with the green and economical method for synthesis, should make carbonized peat moss a highly attractive practical NIB anode material.

METHODS

Material Synthesis. The compressed peat moss biomass was purchased from Premier Horticulture Company, Canada (20 kg in pack). Before the synthesis process, impurities (including small wood sticks, coarse stalks of peat moss, etc.) in the peat moss were thoroughly picked out, leaving only the fine peat moss leaves. For the pyrolysis carbonization process, typically 10 g peat moss precursor is loaded in a tubular furnace and carbonized at a range of temperature (600–1400 °C) with argon flow of 100 sccm min⁻¹. The heating rate is 5 min⁻¹. The yield is from 2.5 to 4.5 g. The obtained hard carbon is carefully washed in 20% KOH at 70 °C for 2 h and 2 M HCl at 60 °C for 15 h to remove the impurities. The purified samples are further rinsed by MQ-water and then collected by filtration. After drying at 120 °C for 12 h in a vacuum oven, carbonized peat moss (CPM) is achieved. Some of the CPM specimens are further activated at

300 °C for 3 h (at a heating rate of 5 min⁻¹ in the tubular furnace) in a dry air flow of 50 sccm min⁻¹. The obtained activated peat moss (designated CPM-A) is first ground and then washed with 2 M HCl and MQ-water again before use.

Material Characterization. To investigate the morphology of peat moss precursor, S-3000N SEM with variable working pressure is used. For the morphologies of carbon, a Hitachi S-4800 SEM equipped with field emission gun is used. TEM analysis is performed using a JEOL JEM-2010 TEM, with an accelerating voltage of 200 kV. The surface area and porous structure are characterized by nitrogen adsorption at 77 K with a Quantachrome Autosorb⁻¹. The samples were outgassed at 250 °C for 4 h under a vacuum prior to the gas sorption measurements. The pore size distributions were evaluated by a nonlocal DFT method using nitrogen adsorption data and assuming slit-pore geometry. XRD analysis was performed using

a Bruker AXS D8 Discover diffractometer with the Cu K α radiation. XPS was obtained on an Axis Ultra spectrometer. All the samples were dried at 120 °C in a vacuum oven overnight to remove the absorbed water before XPS analysis.

Electrochemical Test. Electrochemical tests were carried out using coin cells CR2032. The slurry of 80% active materials, 10% carbon black (Super-P), and 10% poly(vinylidene difluoride) in *N*-methylpyrrolidone was coated on copper foil using a doctor blade and then dried at 110 °C overnight in a vacuum oven, resulting in electrodes with a mass loading of ~1 mg cm⁻². For the samples employed solely for *ex situ* XRD analysis of sodiation-induced lattice dilation, carbon black was not included, and the amount of binder was limited to 5 wt %. Na metal was used as counter electrode and separated from the working electrode with polyethylene separator. The electrolyte was 1 M NaClO₄ dissolved in a mixture of ethylene carbonate (EC) and diethyl carbonate (DEC) with a volume ratio of 1:1. Cyclic voltammetry measurements were conducted on a Solartron 1470 Multistat system. The charge–discharge measurements were performed using an Arbin BT2000 Potentiostat. Electrochemical impedance spectroscopy measurements were also performed using a Solartron 1470E Multichannel Potentiostat/Cell Test System. All electrochemical tests were conducted at room temperature.

Conflict of Interest: The authors declare no competing financial interest.

Acknowledgment. The authors acknowledge financial support from ALMA/AB Bio and NINT NRC.

Supporting Information Available: Figures S1–S15, Tables S1 and S2 as described in the text. This material is available free of charge via the Internet at <http://pubs.acs.org>.

REFERENCES AND NOTES

- Slater, M. D.; Kim, D.; Lee, E.; Johnson, C. S. Sodium-Ion Batteries. *Adv. Funct. Mater.* **2013**, *23*, 947–958.
- Pan, H. L.; Hu, Y. S.; Chen, L. Q. Room-Temperature Stationary Sodium-Ion Batteries for Large-Scale Electric Energy Storage. *Energy Environ. Sci.* **2013**, *6*, 2338–2360.
- Cao, Y. L.; Xiao, L. F.; Wang, W.; Choi, D. W.; Nie, Z. M.; Yu, J. G.; Saraf, L. V.; Yang, Z. G.; Liu, J. Reversible Sodium Ion Insertion in Single Crystalline Manganese Oxide Nanowires with Long Cycle Life. *Adv. Mater.* **2011**, *23*, 3155–3160.
- Yabuuchi, N.; Kajiyama, M.; Iwatake, J.; Nishikawa, H.; Hitomi, S.; Okuyama, R.; Usui, R.; Yamada, Y.; Komaba, S. P2-Type Na_x[Fe_{1/2}Mn_{1/2}]O₂ Made from Earth-Abundant Elements for Rechargeable Na Batteries. *Nat. Mater.* **2012**, *11*, 512–517.
- Shao, Y.; Xiao, J.; Wang, W.; Engelhard, M.; Chen, X.; Nie, Z.; Gu, M.; Saraf, L.; Exarhos, G.; Zhang, J.; et al. Surface-Driven Sodium Ion Energy Storage in Nanocellular Carbon Foams. *Nano Lett.* **2013**, *8*, 3909–3914.
- Senguttuvan, P.; Rousse, G.; Seznec, V.; Tarascon, J. M.; Palacin, M. R. Na₂Ti₃O₇: Lowest Voltage Ever Reported Oxide Insertion Electrode for Sodium Ion Batteries. *Chem. Mater.* **2011**, *23*, 4109–4111.
- Park, Y.; Shin, D. S.; Woo, S. H.; Choi, N. S.; Shin, K. H.; Oh, S. M.; Lee, K. T.; Hong, S. Y. Sodium Terephthalate as an Organic Anode Material for Sodium Ion Batteries. *Adv. Mater.* **2012**, *24*, 3562–3567.
- Zhu, H. L.; Jia, Z.; Chen, Y. C.; Weadock, N.; Wan, J. Y.; Vaaland, O.; Han, X. G.; Li, T.; Hu, L. B. Tin Anode for Sodium-Ion Batteries Using Natural Wood Fiber as a Mechanical Buffer and Electrolyte Reservoir. *Nano Lett.* **2013**, *13*, 3093–3100.
- Darwiche, A.; Marino, C.; Sougrati, M. T.; Fraisse, B.; Stievano, L.; Monconduit, L. Better Cycling Performances of Bulk Sb in Na-Ion Batteries Compared to Li-Ion Systems: An Unexpected Electrochemical Mechanism. *J. Am. Chem. Soc.* **2012**, *134*, 20805–20811.
- Wang, J. W.; Liu, X. H.; Mao, S. X.; Huang, J. Y. Microstructural Evolution of Tin Nanoparticles during *In Situ* Sodium Insertion and Extraction. *Nano Lett.* **2012**, *12*, 5897–5902.
- Zhu, Y. W.; Murali, S.; Stoller, M. D.; Ganesh, K. J.; Cai, W. W.; Ferreira, P. J.; Pirkle, A.; Wallace, R. M.; Cybosz, K. A.; Thommes, M.; et al. Carbon-Based Supercapacitors Produced by Activation of Graphene. *Science* **2011**, *332*, 1537–1541.
- Stoller, M. D.; Park, S. J.; Zhu, Y. W.; An, J. H.; Ruoff, R. S. Graphene-Based Ultracapacitors. *Nano Lett.* **2008**, *8*, 3498–3502.
- Jost, K.; Perez, C. R.; McDonough, J. K.; Presser, V.; Heon, M.; Dion, G.; Gogotsi, Y. Carbon Coated Textiles for Flexible Energy Storage. *Energy Environ. Sci.* **2011**, *4*, 5060–5067.
- Zhang, L. L.; Zhao, X. S. Carbon-Based Materials as Supercapacitor Electrodes. *Chem. Soc. Rev.* **2009**, *38*, 2520–2531.
- Zhao, X.; Hayner, C. M.; Kung, M. C.; Kung, H. H. In-Plane Vacancy-Enabled High-Power Si-Graphene Composite Electrode for Lithium-Ion Batteries. *Adv. Energy Mater.* **2011**, *1*, 1079–1084.
- Winter, M.; Besenhard, J. O.; Spahr, M. E.; Novak, P. Insertion Electrode Materials for Rechargeable Lithium Batteries. *Adv. Mater.* **1998**, *10*, 725–763.
- Linden, D.; Reddy, T. B. *Handbook of Batteries*; McGraw-Hill, Inc.: New York, 2002.
- Dahn, J. R. Phase-Diagram of Li_xC₆. *Phys. Rev. B* **1991**, *44*, 9170–9177.
- Peled, E.; Menachem, C.; BarTow, D.; Melman, A. Improved Graphite Anode for Lithium-Ion Batteries—Chemically Bonded Solid Electrolyte Interface and Nanochannel Formation. *J. Electrochem. Soc.* **1996**, *143*, L4–L7.
- Yang, Z. G.; Zhang, J. L.; Kintner-Meyer, M. C. W.; Lu, X. C.; Choi, D. W.; Lemmon, J. P.; Liu, J. Electrochemical Energy Storage for Green Grid. *Chem. Rev.* **2011**, *111*, 3577–3613.
- Stevens, D. A.; Dahn, J. R. The Mechanisms of Lithium and Sodium Insertion in Carbon Materials. *J. Electrochem. Soc.* **2001**, *148*, A803–A811.
- Stevens, D. A.; Dahn, J. R. High Capacity Anode Materials for Rechargeable Sodium-Ion Batteries. *J. Electrochem. Soc.* **2000**, *147*, 1271–1273.
- Thomas, P.; Billaud, D. Effect of Mechanical Grinding of Pitch-Based Carbon Fibers and Graphite on their Electrochemical Sodium Insertion Properties. *Electrochim. Acta* **2000**, *46*, 39–47.
- Alcantara, R.; Lavela, P.; Ortiz, G. F.; Tirado, J. L. Carbon Microspheres Obtained from Resorcinol-Formaldehyde as High-Capacity Electrodes for Sodium-Ion Batteries. *Electrochim. Solid-State Lett.* **2005**, *8*, A222–A225.
- Komaba, S.; Murata, W.; Ishikawa, T.; Yabuuchi, N.; Ozeki, T.; Nakayama, T.; Ogata, A.; Gotoh, K.; Fujiwara, K. Electrochemical Na Insertion and Solid Electrolyte Interphase for Hard-Carbon Electrodes and Application to Na-Ion Batteries. *Adv. Funct. Mater.* **2011**, *21*, 3859–3867.
- Wenzel, S.; Hara, T.; Janek, J.; Adelhelm, P. Room-Temperature Sodium-Ion Batteries: Improving the Rate Capability of Carbon Anode Materials by Templating Strategies. *Energy Environ. Sci.* **2011**, *4*, 3342–3345.
- Tang, K.; Fu, L. J.; White, R. J.; Yu, L. H.; Titirici, M. M.; Antonietti, M.; Maier, J. Hollow Carbon Nanospheres with Superior Rate Capability for Sodium-Based Batteries. *Adv. Energy Mater.* **2012**, *2*, 873–877.
- Wang, H. G.; Wu, Z.; Meng, F. L.; Ma, D. L.; Huang, X. L.; Wang, L. M.; Zhang, X. B. Nitrogen-Doped Porous Carbon Nanosheets as Low-Cost, High-Performance Anode Material for Sodium-Ion Batteries. *ChemSusChem* **2013**, *6*, 56–60.
- Cao, Y.; Xiao, L.; Sushko, M. L.; Wang, W.; Schwenzer, B.; Xiao, J.; Nie, Z.; Saraf, L. V.; Yang, Z.; Liu, J. Sodium Ion Insertion in Hollow Carbon Nanowires for Battery Applications. *Nano Lett.* **2012**, *12*, 3783–3787.
- Perez, C. R.; Yeon, S. H.; Segalini, J.; Presser, V.; Taberna, P. L.; Simon, P.; Gogotsi, Y. Structure and Electrochemical Performance of Carbide-Derived Carbon Nanopowders. *Adv. Funct. Mater.* **2013**, *23*, 1081–1089.
- Zhang, J. T.; Zhao, X. S. On the Configuration of Supercapacitors for Maximizing Electrochemical Performance. *ChemSusChem* **2012**, *5*, 818–841.
- Titirici, M. M.; Thomas, A.; Yu, S. H.; Muller, J. O.; Antonietti, M. A. Direct Synthesis of Mesoporous Carbons with

Bicontinuous Pore Morphology from Crude Plant Material by Hydrothermal Carbonization. *Chem. Mater.* **2007**, *19*, 4205–4212.

33. Bain, C. G.; Bonn, A.; Stoneman, R.; Chapman, S.; Coupar, A.; Evans, M.; Gearey, B.; Howat, M.; H.; Keenleyside, C.; Labadz, J.; et al. *IUCN UK Commission of Inquiry on Peatlands*; IUCN UK Peatland Programme: Edinburgh, U.K., 2011.

34. Plank, N. The Nature of Cellulose in Sphagnum. *Am. J. Bot.* **1946**, *33*, 335–337.

35. Dahn, J. R.; Zheng, T.; Liu, Y. H.; Xue, J. S. Mechanisms for Lithium Insertion in Carbonaceous Materials. *Science* **1995**, *270*, 590–593.

36. Bold, H. C. *Morphology of Plants*; Joanna Cotler Books: New York, 1967; pp 225–229.

37. Klemm, D.; Heublein, B.; Fink, H. P.; Bohn, A. Cellulose: Fascinating Biopolymer and Sustainable Raw Material. *Angew. Chem., Int. Ed.* **2005**, *44*, 3358–3393.

38. Kim, D. Y.; Nishiyama, Y.; Wada, M.; Kuga, S. Graphitization of Highly Crystalline Cellulose. *Carbon* **2001**, *39*, 1051–1056.

39. Wu, Y. P.; Wan, C. R.; Jiang, C. Y.; Fang, S. B.; Jiang, Y. Y. Mechanism of Lithium Storage in Low Temperature Carbon. *Carbon* **1999**, *37*, 1901–1908.

40. Warren, B. E. X-Ray Diffraction Study of Carbon Black. *J. Chem. Phys.* **1934**, *2*, 551–555.

41. Kercher, A. K.; Nagle, D. C. Microstructural Evolution during Charcoal Carbonization by X-Ray Diffraction Analysis. *Carbon* **2003**, *41*, 15–27.

42. Portet, C.; Yushin, G.; Gogotsi, Y. Electrochemical Performance of Carbon Onions, Nanodiamonds, Carbon Black and Multiwalled Nanotubes in Electrical Double Layer Capacitors. *Carbon* **2007**, *45*, 2511–2518.

43. Yamauchi, S.; Kurimoto, Y. Raman Spectroscopic Study on Pyrolyzed Wood and Bark of Japanese Cedar: Temperature Dependence of Raman Parameters. *J. Wood Sci.* **2003**, *49*, 235–240.

44. Eda, G.; Chhowalla, M. Chemically Derived Graphene Oxide: Towards Large-Area Thin-Film Electronics and Optoelectronics. *Adv. Mater.* **2010**, *22*, 2392–2415.

45. Su, C. Y.; Xu, Y. P.; Zhang, W. J.; Zhao, J. W.; Tang, X. H.; Tsai, C. H.; Li, L. J. Electrical and Spectroscopic Characterizations of Ultra-Large Reduced Graphene Oxide Monolayers. *Chem. Mater.* **2009**, *21*, 5674–5680.

46. Shojaee, S. A.; Zandiashbar, A.; Koratkar, N.; Lucca, D. A. Raman Spectroscopic Imaging of Graphene Dispersion in Polymer Composites. *Carbon* **2013**, *62*, 510–513.

47. Byrne, C. E.; Nagle, D. C. Carbonization of Wood for Advanced Materials Applications. *Carbon* **1997**, *35*, 259–266.

48. Sharma, R. K.; Wooten, J. B.; Baliga, V. L.; Lin, X. H.; Chan, W. G.; Hajaligol, M. R. Characterization of Chars from Pyrolysis of Lignin. *Fuel* **2004**, *83*, 1469–1482.

49. Iyama, K.; Lam, T. B. T.; Stone, B. A. Covalent Cross-Links in the Cell-Wall. *Plant Physiol.* **1994**, *104*, 315–320.

50. Chabannes, M.; Ruel, K.; Yoshinaga, A.; Chabbert, B.; Jaumeau, A.; Joseleau, J. P.; Boudet, A. M. *In Situ* Analysis of Lignins in Transgenic Tobacco Reveals a Differential Impact of Individual Transformations on the Spatial Patterns of Lignin Deposition at the Cellular and Subcellular Levels. *Plant J.* **2001**, *28*, 271–282.

51. Ando, Y.; Zhao, X.; Shimoyama, H. Structure Analysis of Purified Multiwalled Carbon Nanotubes. *Carbon* **2001**, *39*, 569–574.

52. Park, Y. S.; Choi, Y. C.; Kim, K. S.; Chung, D. C.; Bae, D. J.; An, K. H.; Lim, S. C.; Zhu, X. Y.; Lee, Y. H. High Yield Purification of Multiwalled Carbon Nanotubes by Selective Oxidation during Thermal Annealing. *Carbon* **2001**, *39*, 655–661.

53. Cao, Y. L.; Xiao, L. F.; Ai, X. P.; Yang, H. X. Surface-Modified Graphite as an Improved Intercalating Anode for Lithium-Ion Batteries. *Electrochim. Solid-State Lett.* **2003**, *6*, A30–A33.

54. Flandrois, S.; Simon, B. Carbon Materials for Lithium-Ion Rechargeable Batteries. *Carbon* **1999**, *37*, 165–180.

55. Mao, Y.; Duan, H.; Xu, B.; Zhang, L.; Hu, Y. S.; Zhao, C. C.; Wang, Z. X.; Chen, L. Q.; Yang, Y. S. Lithium Storage in Nitrogen-Rich Mesoporous Carbon Materials. *Energy Environ. Sci.* **2012**, *5*, 7950–7955.

56. Wang, Z. H.; Qie, L.; Yuan, L. X.; Zhang, W. X.; Hu, X. L.; Huang, Y. H. Functionalized N-Doped Interconnected Carbon Nanofibers as an Anode Material for Sodium-Ion Storage with Excellent Performance. *Carbon* **2013**, *55*, 328–334.

57. Barsoukov, E.; Kim, J. H.; Kim, J. H.; Yoon, C. O.; Lee, H. Kinetics of Lithium Intercalation into Carbon Anodes: *In Situ* Impedance Investigation of Thickness and Potential Dependence. *Solid State Ionics* **1999**, *116*, 249–261.

58. Levi, M. D.; Aurbach, D. Simultaneous Measurements and Modeling of the Electrochemical Impedance and the Cyclic Voltammetric Characteristics of Graphite Electrodes Doped with Lithium. *J. Phys. Chem. B* **1997**, *101*, 4630–4640.

59. Chen, Z.; Augustyn, V.; Jia, X. L.; Xiao, Q. F.; Dunn, B.; Lu, Y. F. High-Performance Sodium-Ion Pseudocapacitors Based on Hierarchically Porous Nanowire Composites. *ACS Nano* **2012**, *6*, 4319–4327.